photonics

MDPI

Article

Modeling and Analysis of Device Orientation, Analog and Digital Performance of Electrode Design for High Speed Electro-Optic Modulator

Tushar Gaur * , Pragya Mishra, Gopalkrishna Hegde and Talabattula Srinivas

Department of Electrical Communication Engineering, Indian Institute of Science, Bangalore 560012, Karnataka, India; pragyamishra@iisc.ac.in (P.M.); gopalkrishna@iisc.ac.in (G.H.); tsrinu@iisc.ac.in (T.S.)

* Correspondence: tushargaur@iisc.ac.in

Abstract: Electro-optic modulators (EOMs) are crucial devices for modern communication enabling high bandwidth optical communication links. Traveling wave electrodes are used to obtain high-speed modulation in these EOMs. We present the electrode design and analysis along with the study of effects of changing orientation on device performance for a thin-film lithium niobate tunable Mach–Zehnder interferometer (MZI) that offers sub-THz bandwidth operations. High velocity and impedance matching with low RF attenuation, high third-order SFDR (∼121 dB/Hz$^{2/3}$) and a low half-wave voltage length product (1.74 V.cm) have been achieved for a bandwidth of 136 GHz. High-speed digital modulation using multi-level signal formats (PAM-2, QAM-4 and QAM-16) with low BER for 400 Gbps data has been demonstrated to assess the digital performance of the device.

Keywords: integrated optoelectronic; electrode design; thin-film lithium niobate; higher order modulation; optical communication; sub-THz communication; sub-Tbps communication

check for updates

Citation: Gaur, T.; Mishra, P.; Hegde, G.; Srinivas, T. Modeling and Analysis of Device Orientation, Analog and Digital Performance of Electrode Design for High Speed Electro-Optic Modulator. *Photonics* **2023**, *10*, 301. https://doi.org/10.3390/photonics10030301

Received: 23 January 2023
Revised: 6 March 2023
Accepted: 9 March 2023
Published: 12 March 2023

1. Introduction

Data from Cisco telecommunication suggests that mobile traffic users will grow to 66% of the global population by 2023 [1–4]. This growth, along with most countries opting for green energy, advocates the shift towards the optical mode of communication, which solves the electric bottleneck by offering high bandwidth, low power consumption and a smaller footprint [2–4].

Over the years, scientists and research groups have investigated various techniques such as thermo-optic effects, free-carrier plasma dispersion, micro-optoelectromechanical systems (MOEMS) and electro-optic effects for enabling high-speed optical modulation [4–11]. Among these, modulators based on the thermo-optic effect suffer from slow response time (5–200 µs), while the performance of plasma-dispersion-based modulators is hindered by coupled attenuation losses with phase change. MOEMS devices offer a small footprint and low crosstalk; however, they require high operating voltages and are incompatible with CMOS technology. The electro-optic effect allows a faster response with no coupled attenuation and offers CMOS-compatible platforms. Among these platforms, x-cut thin-film lithium niobate (TFLN) has drawn significant attention as it provides a wide transparent window, high-temperature stability, a high refractive index contrast, a large bandwidth, low optical losses, a large Pockel's coefficient and narrow gap electrodes reducing the half-wave voltage (V_π) [2,11].

To meet the modern communication demands, modulators must be designed for high bandwidth operations considering fabrication limitations and tolerances. In high-speed TFLN-based modulators coplanar waveguide traveling wave electrodes allowing push–pull configuration is used. This is due to the large length of the phase shifters compared to the wavelength [12]. To obtain THz operation, electrode design needs to be precise,

taking care of the three primary factors: (i) velocity matching, (ii) impedance matching and (iii) low RF attenuation [13]. With accurate design technology and maturity in TFLN MZI fabrication, the performance metric of the device can be predicted reliably. EOM performance is investigated through the figures of merit (FOM) defined by half-wave voltage and length product $(V_\pi L)$, modulation bandwidth and modulation efficiency. Maturity in fabrication technology allows fabrication of multiple devices on a compact chip specially for space and defence applications which require fabrication of device in various orientations. Multiple device orientations are also common in programmable photonic circuits. However, due to the inherent anisotropy of lithium niobate, the device performance is bound to be affected by a change in orientation of the device, which makes analyzing the effects of orientation on the device's performance essential. Apart from these, assessing the device's intermodulation distortion and digital performance is necessary to implement the modulator in practical communication links. Intermodulation distortions (IMD) are unavoidable due to the inherent nonlinearity associated with the optical modulators. Thus, the spurious free detection range (SFDR) calculation quantifying the device's nonlinearity becomes an important FOM. Bulky conventional lithium niobate (LN) modulators offer a high SFDR of around 110–120 dB/Hz $^{2/3}$, compared to etched LN waveguide modulators with an SFDR of around 97.2 dB/Hz$^{2/3}$ [14]. Suppressing IMDs in optical modulators is challenging, and various linearization techniques [15–17] are utilized to improve SFDR. However, these are out of the scope of this article. Modern-day communication links such as 5G/6G, satellite communication and multi-system operators in the television industry utilize digital communication to transmit information. To keep pace with growth in data traffic demands, future terabit links require higher order modulation (multi-level signals) to increase the spectral efficiency and channel bandwidth compared to on–off keying (OOK) in long-haul transmission links. Thus, it becomes necessary to analyze the digital performance of the modulators, which is estimated by a clearly distinguishable constellation and low bit error rate (BER).

Recently, many authors have proposed a variety of (different) designs for high-speed MZI electro-optic modulators (EOM) [12,18–23]. However, most of these designs have bandwidths limited to below the sub-THz domain, and do not discuss the effects of device orientation, distortion analysis and digital performance of the device. They also do not provide an option for microvia connections, which become essential for thin electrode designs. In this work, we propose the ultrathin-film electrode design along with the study of the effects of orientation on device performance, SFDR and digital performance calculation for high bandwidth and low $V_\pi L$ EOMs, targeting futuristic applications in aerospace, photonic RADAR, telecommunication and satellite communication industries. This paper is divided into five sections; the effects of various design parameters have been analyzed in detail in the design section, and the study of alteration in material and electro-optic parameters with change in orientation of the device has been described in the effects of orientation section. The theory of intermodulation distortion has been presented in the distortion calculation section. Electro-optic and radio frequency (RF) responses, along with modulation efficiency, $V_\pi L$, SFDR and digital performance of the proposed novel design have been analyzed in the results section. A comparison with recently proposed devices in the literature and a summary are conferred in the discussion.

2. Design

The electro-optic modulator uses a coplanar waveguide (CPW) traveling wave electrode design in the push–pull configuration on the x-cut TFLN platform. Based on the market specifications of available lithium niobate on insulator (LNOI) wafers, a substrate with a buried oxide layer (SiO_2) thickness of 4.7 μm is selected. Directly etched lithium niobate (LN) ribs on the LN layer are used for light propagation, and the RF field is applied via gold electrodes deposited on a SiO_2 buffer layer, such that the applied field aligns along the z-axis to utilize the strongest Pockel's coefficient ($r_{33} = 30$ pm/V). A cladding is provided to guard the device against environmental damage and support microvia connectors [14,24]. Figure 1 shows the

cross-section and the top view of the device, and Table 1 enlists the different dimensions displayed in the figure.

Table 1. Dimensions of various layers displayed in Figure 1.

t_{LIN}	h_{rib}	w_{rib}	t_{Buffer}	t_{Au}	h_{clad}	h_{BOX}	h_{Si}
0.3 µm	0.4 µm	1.25 µm	0.2 µm	0.5 µm	2.75 µm	4.7 µm	500 µm

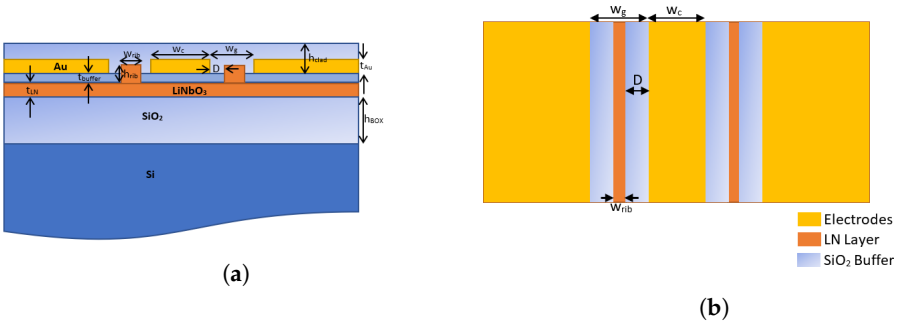

(**a**) (**b**)

Figure 1. (**a**) Cross section and (**b**) top view of the proposed electro-optic modulator.

Parameters deciding the performance metric of the electro-optic modulator depend on the regular coplanar waveguide line's characteristic impedance, effective indices and RF losses, which are decided by dimensions listed in Table 1. Among these dimensions, BOX thickness, and silicon layer thickness are fixed by the manufacturer (in our case). Dimension of rib and the LN layer are decided to obtain single mode operation and electrode thickness is fixed at 0.5 µm. Buffer thickness is kept at 0.2 µm, as a thicker buffer will affect the elecrtric field distribution and a thinner buffer layer leads to increase in metal-induced optical losses. Thus, we are left with h_{clad}, trace width (w_c), electrode gap (w_g), rib distance (D) and electrode thickness (t_{Au}). These parameters should be optimized for a high bandwidth operation at a low half-wave voltage (V_π) to achieve maximum velocity matching ($\Delta n = n_{eff} - n_{op}$), impedance matching ($R = (Z_{in} - Z_L)/(Z_{in} + Z_L)$) and low microwave losses. Here n_{eff}, Z_{in} and n_{op} are the effective RF refractive index, input line impedance and optical group index, respectively. Microwave losses are governed by three types of losses in CPW traveling wave electrodes: conductor losses, dielectric losses and radiation losses [12,25,26]. Conductor losses are decided by skin depth and vary as a square root function of frequency; dielectric losses are calculated using loss tangent and vary as a linear function of frequency. Radiation losses depend on the surface roughness of the metal electrodes. Optimized fabrication techniques allow the RMS surface roughness value to be constrained within a few nanometers [27,28]; thus, the effects of surface roughness are neglected in device modeling considering the plain electrode deposition [12,21,22]. At an RF frequency of 100 GHz, w_c and w_g are varied for different h_{clad} to study the variation in n_{eff}, Z_o and RF losses of CPW using COMSOL multiphysics solver. Equivalent optical mode group index for different values of h_{clad} were obtained. After a critical optimization, h_{clad} was decided to be 2.75 µm, and corresponding results are shown in Figure 2.

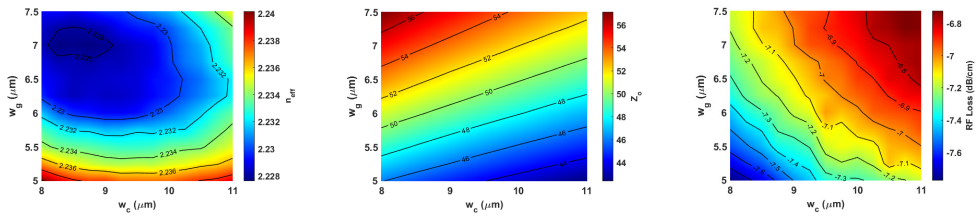

(**a**) (**b**) (**c**)

Figure 2. Color maps of (**a**) n_{eff}, (**b**) Z_o and (**c**) RF losses for varying w_c and w_g at t_{Au} = 0.5 µm and h_{clad} = 2.75 µm.

An optical mode group index (n_{op}) of 2.238 was obtained based on the dimensions used in the simulations. In order to have high velocity and impedance matching, n_{eff} and Z_o should be kept near n_{op} and 50 Ω, respectively. As evident in Figure 2, the n_{eff} varies around an obtained n_{op} between 2.228 and 2.24, while Z_o varies between 44 Ω and 56 Ω.

Another critical factor deciding the performance metric of the MZI is $V_\pi L$ which depends on w_g, overlap factor (τ), the extraordinary refractive index of $LiNbO_3$ (n_e = 2.138), and optical wavelength (λ_o) and is given by

$$V_\pi L = \frac{\lambda_o w_g}{2\pi n_e^3 r_{33} \tau} \tag{1}$$

where τ is given by

$$\tau = \frac{w_g}{V} \frac{\iint \mid E_{op} \mid^2 E_{rf} dS}{\iint \mid E_{op} \mid^2 dS} \tag{2}$$

τ depends on the RF and optical field along the z-axis and the rib distance D from the trace electrode. Using the RF and optical fields, the overlap integral is calculated using Equation (2) for varying rib distance from the trace electrode and is plotted in Figure 3a. Results suggest that as we move away from the trace electrode, the value of τ decreases toward the center of the electrode gap, and then starts increasing gradually as we move towards the ground due to the increase in RF field toward the ground electrode. As we place the rib closer to the trace electrode, the metal-induced losses in the optical mode increase. This issue is addressed by depositing a SiO_2 buffer layer between the electrodes and the LN layer. Variation of $V_\pi L$ with D is plotted in Figure 3b. From the results, the value of D was determined to be 1.6 μm; at this position, the value of τ is 0.87.

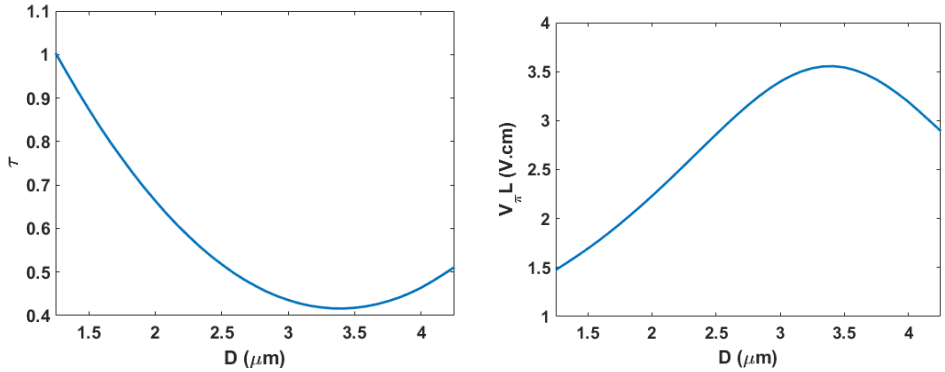

Figure 3. (**a**) τ and (**b**) $V_\pi L$ for varying rib placement for w_c = 8.25 μm and w_g = 5.75 μm.

3. Effects of Orientation

Due to the inherent anisotropy of the LiN material, the RF dielectric constant, optical refractive index and effective Pockel's coefficient change with the orientation of the device. Change in the RF dielectric constant and effective refractive index results in the change in RF electric field distribution and optical mode distribution within the structure, affecting the overlapping factor.

In order to quantify the effects of orientation on the effective Pockel's coefficient of the device, the device is rotated by an angle θ as shown in Figure A1. An x-cut LiN has axes given by x, y and z, with unit vectors denoted as $\hat{x}$, $\hat{y}$ and $\hat{z}$. Under the effect of rotation the new axes are represented as x′, y′ and z′, with unit vectors $\hat{x'}$, $\hat{y'}$ and $\hat{z'}$. The rotation matrix for the transformation is thus given by

$$R_\theta = \begin{bmatrix} 1 & 0 & 0 \\ 0 & cos(\theta) & sin(\theta) \\ 0 & -sin(\theta) & cos(\theta) \end{bmatrix} \tag{3}$$

Since dielectric (ϵ) and perturbation ($\Delta\epsilon$) are tensors, under the effect of rotation new dielectric and perturbation tensors are given as

$$[\epsilon'] = R_\theta \begin{bmatrix} \epsilon_{11} & 0 & 0 \\ 0 & \epsilon_{22} & 0 \\ 0 & 0 & \epsilon_{33} \end{bmatrix} R_\theta^{-1} \tag{4a}$$

$$[\Delta\epsilon'] = R_\theta \begin{bmatrix} \Delta\epsilon_{11} & 0 & 0 \\ 0 & \Delta\epsilon_{22} & 0 \\ 0 & 0 & \Delta\epsilon_{33} \end{bmatrix} R_\theta^{-1} \tag{4b}$$

$$\begin{aligned} \Delta\epsilon_{11} &= -\epsilon_{11}^2(r_{13}E_{rf}) \\ \Delta\epsilon_{22} &= -\epsilon_{22}^2(r_{23}E_{rf}) \\ \Delta\epsilon_{33} &= -\epsilon_{33}^2(r_{33}E_{rf}) \end{aligned} \tag{4c}$$

Combining the Equations in (4a) and (4b), the new perturbation is written as

$$\Delta\epsilon_{33} = sin^2(\theta)\Delta\epsilon_{22}^2 + cos^2(\theta)\Delta\epsilon_{33}^2 \tag{5}$$

Using the above relations the change in effective refractive index as a function of θ is given by

$$\Delta n_{eff}(\theta) = n_{eff_o}\left(\epsilon_{33}^2 r_{33} cos^3(\theta) + \epsilon_{22}^2(r_{22}sin(\theta) + r_{23}cos(\theta))sin^2(\theta)\right) \tag{6}$$

Similar equations are derived for the y-cut LiN platform using the same concept as described in Equations (3)–(6). The normalized change in refractive index with orientation angle while neglecting the effects of change in RF and optical field distribution are plotted in Figure 4a.

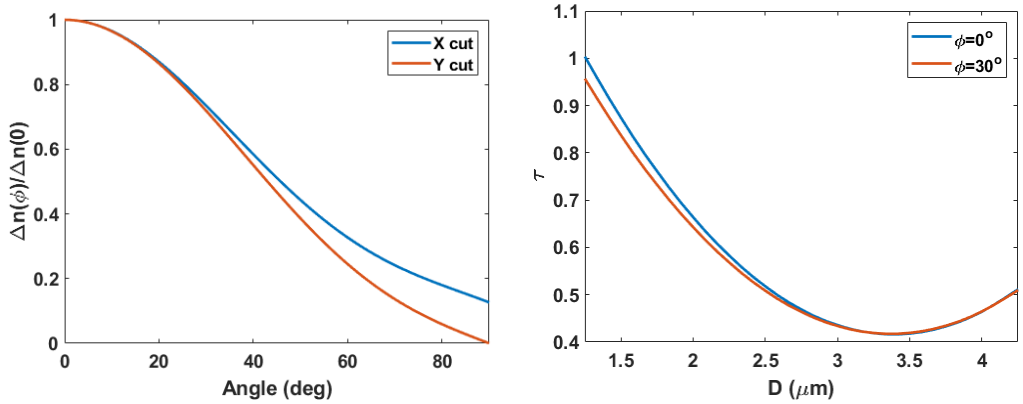

(**a**) (**b**)

Figure 4. Change in (**a**) refractive index (neglecting the change in τ) and (**b**) τ for varying D.

However, due to the anisotropic behaviour of LiN, the RF dielectric constant and optical refractive index changes with the orientation of the device. This results in a change in the distribution of RF and optical field, varying the overlap factor τ. Variation in the (τ) for an orientation of 30° is depicted in Figure 4b. The results in the figure suggest that τ reduces by a factor of 0.91 (at the previously determined value of D) due to the change in field distribution within the structure.

4. Distortion Calculation

When the photodetector is illuminated with light from EOM, the resulting photocurrent is given as

$$I_{detect} = e^{-\alpha L}\frac{P_{In}R_d}{2}\left(1 - cos\left(T_o + \frac{\pi}{V_\pi}v_{rf}(t)\right)\right) \tag{7}$$

Here α, P_{in}, R_d, T_o and $v_{rf}(t)$ are the waveguide attenuation constant, input optical power, photodetector responsivity, bias point and modulator driving voltage, respectively. Since the output is in terms of cosine, the nonlinearity which gives rise to higher order distortions, in this case, is sinusoidal. The distortion performance of an electro-optic modulator in an optical link can be measured and compared using a commonly employed two-tone test, which applies two equal amplitude signals at two closely spaced RF frequencies (ω_1 and ω_2). For small signal RF input, the first order terms grow linearly while the third order term grows cubically with the input RF power. Output power in all the orders can be predicted by rewriting Equation (7) using Bessel function expansion while applying input RF signal $v_{rf}(t) = v_1 sin(\omega_1 t) + v_2 sin(\omega_2 t)$.

$$I_{detect} = e^{-\alpha L}\frac{P_{In}R_d}{2}\left(1 - cos\left(T_o + \frac{\pi}{V_\pi}(v_1 sin(\omega_1 t) + v_2 sin(\omega_2 t))\right)\right) \tag{8a}$$

$$= Re\left\{exp(jT_o)\sum_n\sum_m J_n\left(\frac{\pi v_1}{V_\pi}\right)J_m\left(\frac{\pi v_2}{V_\pi}\right)exp(j(n\omega_1 t + m\omega_2 t))\right\} \tag{8b}$$

where n,m = 0, ±1, ±2 …

$$= \begin{cases} cos(T_o)J_0\left(\frac{\pi v_1}{V_\pi}\right)J_0\left(\frac{\pi v_2}{V_\pi}\right) & \text{for n = 0, m = 0} \\ (\pm 1)^n 2cos(T_o)J_n\left(\frac{\pi v_1}{V_\pi}\right)J_m\left(\frac{\pi v_2}{V_\pi}\right)cos(n\omega_1 t + m\omega_2 t) & \\ & \text{for n + m = even} \\ (\pm 1)^{n+1} 2cos(T_o)J_n\left(\frac{\pi v_1}{V_\pi}\right)J_m\left(\frac{\pi v_2}{V_\pi}\right)sin(n\omega_1 t + m\omega_2 t) & \text{for n + m = odd} \end{cases} \tag{8c}$$

The maximum magnitude of the fundamental signal ($P_{max(i)}$) that a link can convey without any measurable distortion of a particular order (i) is when the power of modulation-produced distortion of that order is equal to the noise power. This is termed as $SFDR_i$ and can be expressed as

$$SFDR_i = P_{max(i)} - N\,|_{dB} \tag{9}$$

Noise at the detector of an optical link is given as the addition of noise generated at the RF input of the modulator, additional noise at the detector (generally given by shot noise) and relative intensity noise (RIN) of the laser. Noise in dB is given as

$$\begin{aligned} N &= N_{in} + N_{add} + N_{RIN} \\ &= 10log_{10}\left(G_i KT + < i_{shot} >^2 R_{LOAD} + I_D^2 R_d 10^{\frac{N_{RIN}}{10}}\right) \\ &= 10log_{10}\left(e^{-\alpha L}\frac{P_{in}\pi R_s}{2V_\pi}R_d Kt + 2qI_D R_{LOAD} + I_D^2 R_d 10^{\frac{N_{RIN}}{10}}\right) \end{aligned} \tag{10}$$

Here G_i is the gain of the link, Rs is the input resistance, K is Boltzman's constant, T is the temperature (290 K), $I_D = P_{in}R_d/2$, R_{LOAD} is the load resistance and N_{RIN} is the laser intensity noise mentioned by the manufacturer.

5. Results and Discussion

5.1. Electrode Design

Based on the results obtained in Figure 2, optimization was performed to maximize the performance metric of the MZI (Detailed in Appendix A), and values of w_g and w_c were found to be 8.25 µm and 5.75 µm. Using the optimized dimensions for electrodes n_{eff}

(and Δn) and Z_0 (Z_{in} and R) versus RF frequency are plotted in Figure 5a,b, respectively. Here, Z_{in} is the input line impedance calculated using the Equation in [12]. It is evident that n_{eff} and Z_o decrease sharply in the sub-GHz region and remain very close to n_{op} and 50 Ω, respectively, in the sub-THz region, providing high velocity and impedance matching. Δn, Z_{in} and R further verify the results plotted in figures.

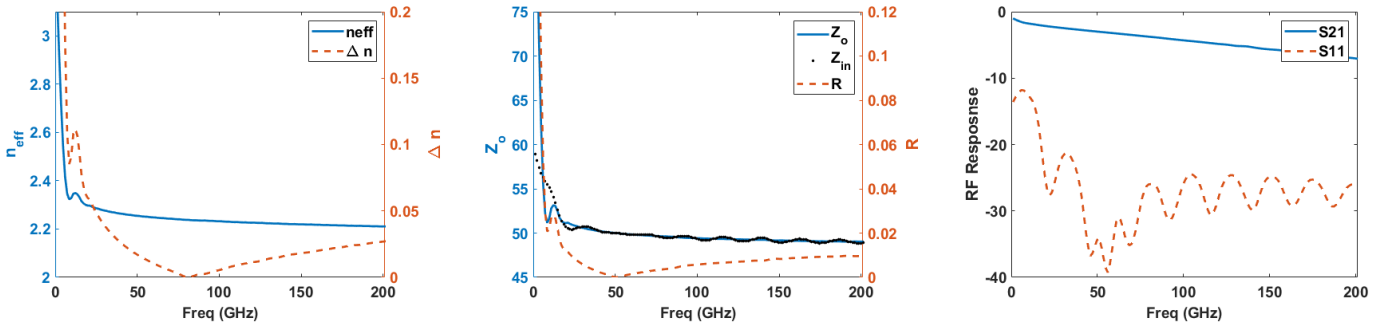

(**a**) (**b**) (**c**)

Figure 5. (**a**) n_{eff} (and Δn), (**b**) Z_o (Z_{in} and R) and (**c**) RF response of the CPW for the design parameters versus RF frequency.

Apart from velocity and impedance matching, the MZI bandwidth also depends on the RF response of the electrode lines. As the length (L) increases, the RF losses increase, which hinders the performance of the MZI. The result in Figure 3b suggests that $V_\pi L$ for the proposed design is 1.74 V.cm. Using this result, the RF response of the designed electrodes for L = 2.9 mm is plotted against the RF frequency in Figure 5c. The figure shows that S_{21} remains moderately above −10 dB at 200 GHz and S_{11} remains around −30 dB for the complete RF frequency range.

The electro-optic and RF responses are plotted together in Figure 6a. The figure also displays the electro-optic and RF bandwidths of the proposed device. The 3 dB electro-optic bandwidth for the proposed device is 136 GHz. Modulation efficiency and phase error (refer to Appendix A Equations (A5)) are plotted in Figure 6b, and it remains at −1.24 dB at the maximum bandwidth, while phase error remains below 0.08 rad (4.6°). Due to deterioration of electro-optic transmittance with frequency, $V_\pi L$ also changes with frequency. Variation of $V_\pi L$ against the RF frequency is plotted in Figure 6c. The figure shows that $V_\pi L$ increases with the RF frequency. Since L is fixed, it means that the V_π of the device changes with the frequency. The performance of various CPW-based TFLN modulators has been listed in Table 2.

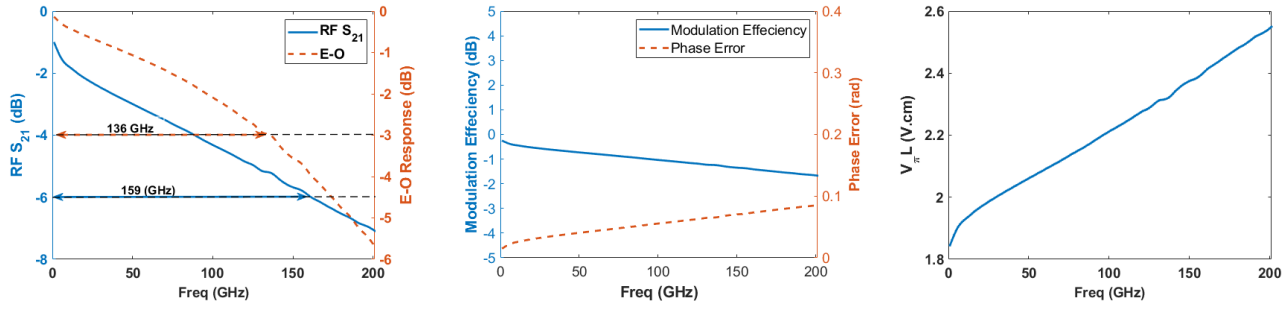

(**a**) (**b**) (**c**)

Figure 6. (**a**) RF (S_{21}) and electro-optic response, (**b**) modulation efficiency and phase error and (**c**) $V_\pi L$ versus RF frequency.

Table 2. Performance comparison of various CPW-based TFLN modulators.

Paper	$V_\pi L$ (V.cm)	Electrooptic Bandwidth (GHz)	L (mm)	V_π (V)
[12] (theo.)	2.93	<100	3	9.76
[18] (exp.)	2.2	100	5	4.74
[19] (exp.)	2.5	70	5	5.1
[20] (exp.)	6.7	106	5	13
[21] (theo.)	3.7	29	24	1.3
[22] (exp.)	1.75	40	5	3.5
[23] (theo.)	2.32	81	30	1.16
This work	1.74	136	2.9	6

5.2. Orientation

Effective RF index for varying frequency and optical mode index is calculated for the two orientations (0° and 30°). Using Equations (3)–(6), values for effective Pockel's coefficients are calculated, and using the results in Figure 4, $V_\pi L$ is calculated by substituting the values in Equation (1). $V_\pi L$ and $\Delta V_\pi L$ are plotted against the D and RF frequency for the two orientations in Figure 7. The results obtained in Figure 7a show that $\Delta V_\pi L$ increases initially with D toward the center of w_g and then reduces. These results are consistent with the results obtained in Figure 4b. It is evident from the results in Figure 7b that to maintain the same order of performance in the device rotated by an angle of 30°, the V_π increases. $\Delta V_\pi L$ also increases due to increase in the difference between effective RF and optical mode index with the frequency.

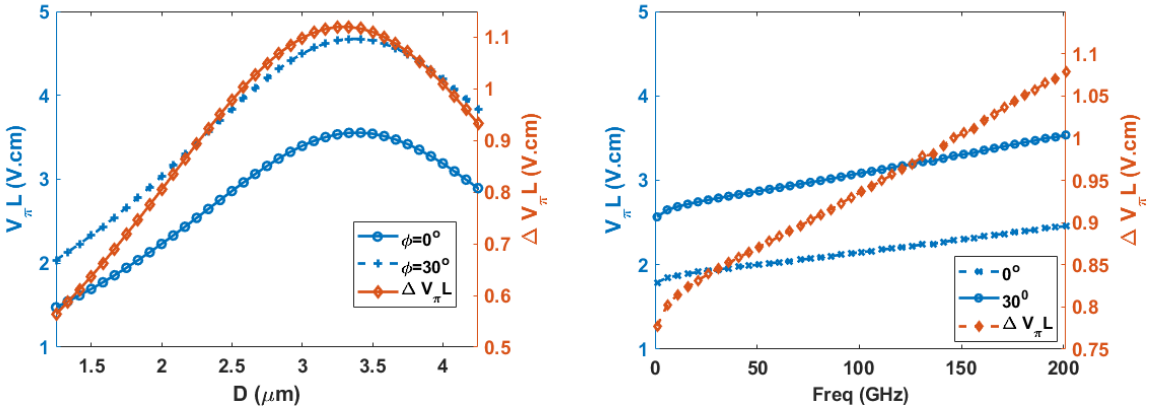

Figure 7. $V_\pi L$ and $\Delta V_\pi L$ for 0° and 30° versus (**a**) D and (**b**) RF frequency.

5.3. SFDR Calculation

For SFDR measurement, we consider R_s and R_{LOAD} to be 50 Ω, waveguide attenuation and P_{in} to be 0.2 dB/cm and 25 mW, respectively, and R_d as 0.85 A/W. V_π is taken from the calculations in the electrode design section. Laser relative intensity noise is 165 dB/Hz, according to the laser data sheet [29]. Operating temperature T is 290 K. Using these values, a noise floor of −179 dB is obtained at 1 Hz. RF output power in fundamental, IMD2 and IMD3 signals is calculated for $v_1 = v_2 = 1$ V with varied biasing voltage and plotted against the biasing angle in Figure 8a. The figure depicts at quadrature biasing that IMD2 is eliminated as suggested in Equation (4c). As the biasing angle increases towards 180°, a decrease in IMD3 output power is also observed. To eliminate IMD3, the biasing point can be kept near 180° if the signals are wide apart so that IMD2 can be filtered out using a low-power RF filter. However, using the quadrature bias point, RF output of fundamental and IMD3 signals are plotted with NF for varying inputs of RF power in Figure 8b. Using Equation (5), SFDR3 is calculated and depicted in the figure as 121 dB/Hz$^{2/3}$.

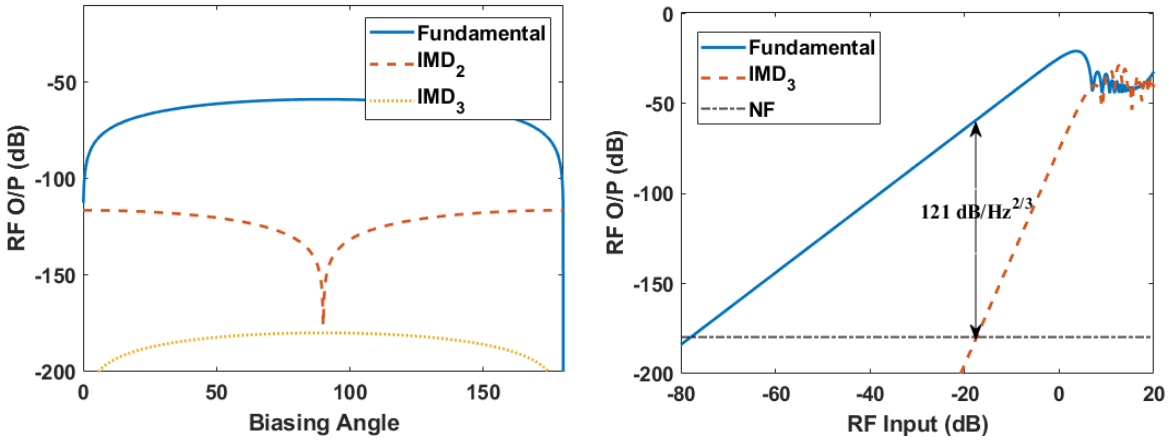

Figure 8. (**a**) Fundamental, IMD2 and IMD3 RF output at the detector versus biasing angle and (**b**) fundamental, IMD3 and noise floor RF output versus RF input power.

5.4. Digital Modulation Performance

To assess the digital modulation performance, the proposed device is tested with pulse amplitude and quadrature amplitude modulations (PAM-2, QAM-4 and QAM-16). Pseudo-random binary signals varying from 10 Gbps to 400 Gbps with 100 samples per bit are generated (considering bitrate equal to twice the bandwidth of operation) and mapped to PAM-2, QAM-4 and QAM-16 to form modulating signals. Pulse shaping is performed using a raised cosine filter with a roll-off factor of 0.01, and the peak-to-peak voltage of 4 V is maintained for all the signals. These signals are passed through the traveling wave electrode, whose filter response is estimated from the obtained frequency response (see Appendix A.4) and then given to the proposed EOM, operating at the quadrature biasing point $(V_\pi/2)$. Biasing voltage is varied with regard to the bit rate from 3 V to 4.2 V. For PAM-2 modulation, a single MZI is used, while for QAM-4 and QAM-16 modulations, a dual-parallel Mach–Zehnder scheme is followed [30,31]. An OSNR of 25 dB is considered while obtaining the output from the downsampled signal at the detector to generate the constellation diagrams shown in Figure 9. The figure shows the reference point (red), received signal constellation at the output of EOM (green) and received signal constellation at the output of detector (blue). A slight deviation and scattering in the constellation at the output of EOM (green) can be observed; this is due to the low-pass filtering effect induced by the traveling wave electrodes (which induce ripples in the waveform) and velocity and impedance mismatch. In this case, the filtering effect is the dominating factor for this deviation. The output signal is applied to a decision maker to recover the transmitted bits after eliminating eight samples from the start and the end. For BER estimation, bitrates equal to the bandwidth are considered and applied to the device. The BER of 0 is obtained at all the data rates for PAM-2 and QAM-4 modulation. BER for QAM-16 modulations is presented in Figure 10 (blue). The figure shows that the BER increases for lower data rates as well due to reduced V_π, which causes an imbalance of applied voltage between the outer and the inner constellations. BER, in these cases, can be improved by manipulating the applied voltages for the inner constellation such that these constellations move towards the center while keeping outer constellations intact at their positions. Values of improved BER by scaling the voltages of the inner constellation by 0.83 are also plotted in the figure (orange). As observed in the figure, the BER increases rapidly as the device's bandwidth (136 GHz) is crossed, and at 150 Gbps (150 GHz), the BER increases to 1.8×10^{-3} . At the bitrate of 400 Gbps (100 GHz), a BER of 1.8×10^{-3} is obtained, which is below the hard decision forward error correction (HD-FEC) threshold.

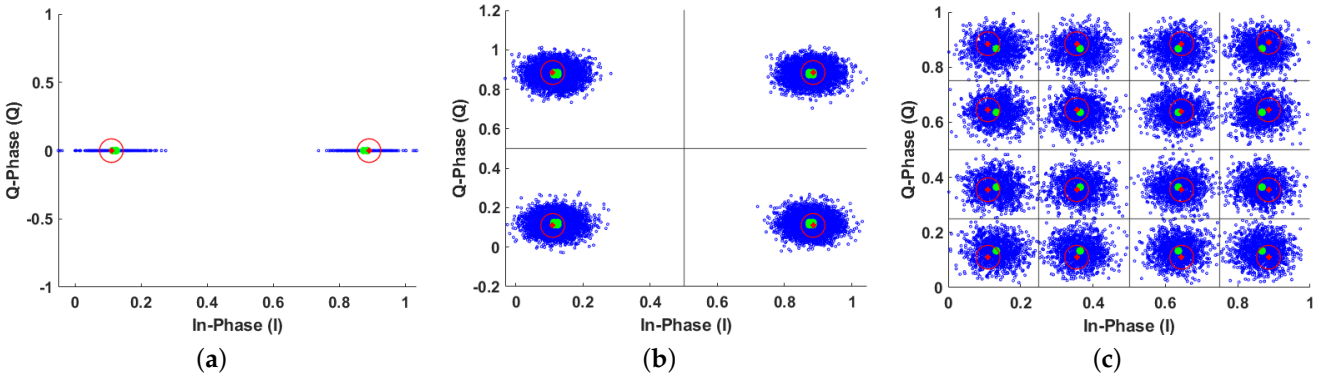

Figure 9. Constellation diagram for (**a**) PAM-2, (**b**) QAM-4 and (**c**) QAM-16 signals. Red is the reference, green is received signal without OSNR and blue is received signal with OSNR at 200 Gb/s (100 GHz).

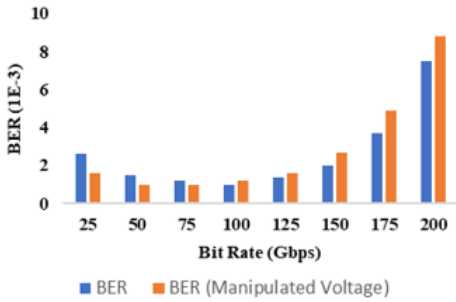

Figure 10. BER performance for varying bit rates with and without manipulated voltages.

6. Conclusions

A compact TFLN modulator maintaining high bandwidth, high modulation efficiency, low phase error and low $V_\pi L$ meeting the fabrication limits has been proposed. The results suggest that the change in orientation of the device majorly impacts the electro-optic response, while effects on RF response are negligible. To meet the performance of a non-rotated device, $V_\pi L$ of the rotated device increases. SFDR calculations have been performed for varying bias voltage and input RF power to quantify the nonlinearity. An SFDR3 of 121 dB/Hz$^{2/3}$ is obtained, which is comparable with the high SFDR of conventional LN modulators. SFDR performance of the device can be further enhanced as high as 135 dB/Hz$^{2/3}$ by using various linearization techniques available in the literature. The digital performance of the proposed device is analyzed at varying bit rate random binary signal for multi-level higher order modulation schemes. A BER well below the HD-FEC threshold is obtained for 400 Gbps at 100 GHz enabling 400 G communication. Thus, the proposed device shows great potential for applications in state-of-the-art communication technology (5G/6G, satellite downlink, RADAR, etc.) by offering a bandwidth >100 GHz with a high SFDR and low BER for a sub-terabit link. The design and analysis method used in this article is not limited to the LNOI platform only but can also be extended to other hybrid platforms. Currently we are working on the process optimization for complete fabrication of the device for verifying our simulation results.

Author Contributions: T.G. conceived the presented idea, developed the theory and performed the computations. T.G. and P.M. verified the analytical methods. T.G., P.M. and G.H. drafted the manuscript and verified the results. T.S. encouraged the investigation of the design and performance of the design. All authors discussed the results and contributed to the final manuscript. All authors have read and agreed to the published version of this manuscript.

Funding: This research is funded by Ministry of Education, Government of India, under Prime Minister's Research Fellowship scheme.

Institutional Review Board Statement: Not applicable

Informed Consent Statement: Not applicable.

Data Availability Statement: Not applicable.

Acknowledgments: We would like to thank Deepak Sharma from Nano-Device and Sensors Laboratory, Department of Centre for Nano Science and Engineering, Indian Institute of Science, for his inputs.

Conflicts of Interest: The authors declare that there are no conficts of interest regarding the publication of this paper.

Sample Availability: Not applicable.

Abbreviations

The following abbreviations are used in this manuscript:

EOM	Electrooptic modulator
MZI	Mach–Zehnder interferometer
SFDR	Spurious free dynamic range
PAM	Pulse amplitude modulation
QAM	Quadrature amplitude modulation
BER	Bit error rate
FOM	Figure of merit
IMD	Intermodulation distortion
TFLN	Thinfilm lithium niobate
CPW	Coplanar waveguide

Appendix A

Appendix A.1. Optimization Method

The MZI performance is measured mainly by velocity matching, impedance matching and RF losses. Velocity mismatch decides the response of electro-optic modulator in terms of the cosine of mismatch factor and is given by Equation (A1). Impedance mismatch causes the reflection of an RF wave from the load and thus degrades the power delivery to the phase shifter and is given by Equation (A2). RF loss is decided by the imaginary part of the RF effective refractive index, which defines the decay of power towards the end of the electrode, and is given by Equation (A3).

$$\alpha_{vel.mismatch} = cos\left(\frac{2\pi\left(n_{eff} - n_{op}\right)}{\lambda_{rf}}L\right) \tag{A1}$$

$$R = \frac{Z_{in} - Z_L}{Z_{in} + Z_L} \tag{A2}$$

$$\alpha_{rf} = exp\left(-\frac{2\pi imag\{n_{eff}\}}{\lambda_{rf}}L\right) \tag{A3}$$

The results for the first equation are squared and subtracted from the maximum value and added to the square of the second and third equations for defining the target function given by

$$Target = \left(\left(1 - \alpha^2_{vel.mismatch}\right)^2 + |R|^2 + (\alpha^2_{rf})\right) \tag{A4}$$

To optimize the value of w_c and w_g, optimization is run across values obtained in Figure 2 to find the minimum value of the target function.

Appendix A.2. Modulation Efficiency

Modulation efficiency and phase error $(\Delta\theta)$ are calculated using the following equations to assess the EOM performance:

$$H\left(\omega_{rf}\right) = \frac{Z_{in}}{Z_{in}+Z_L}\frac{1}{e^{\gamma l}+Re^{-\gamma l}} \times \left[\frac{Sinh\left(\frac{Al}{2}\right)e^{-\frac{Al}{2}}}{\frac{A}{2}} + R\frac{Sinh\left(\frac{Bl}{2}\right)e^{-\frac{Bl}{2}}}{\frac{B}{2}}\right] \tag{A5a}$$

$$A = -\alpha_{rf} - j\left(\beta_{rf} - \beta_{op}\right) \tag{A5b}$$

$$B = \alpha_{rf} - j\left(\beta_{rf} + \beta_{op}\right) \tag{A5c}$$

$$\Delta\theta = \theta - \frac{\pi n_e^3 r_{33}\tau L V_\pi}{\lambda_o}$$

where

$$\theta = \frac{\pi n_e^3 r_{33}\tau L V_\pi}{\lambda_o} H\left(\omega_{rf}\right) \tag{A5d}$$

Modulation efficiency (m) is thus given by

$$m = \frac{H\left(\omega_{rf}\right)}{H(0)} \tag{A5e}$$

Appendix A.3. Rotated Coordinates

Considering an x-cut lithium niobate, the coordinates of an unrotated device are given by y and z in Figure A1, while for the device rotated by an angle θ, the rotated coordinates are represented as y' and z'.

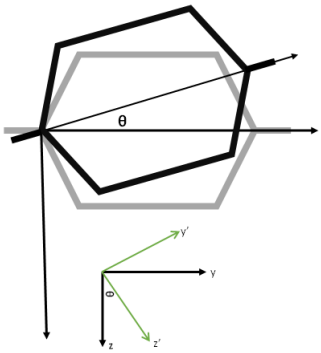

Figure A1. Cross section view of the proposed electro-optic modulator.

Appendix A.4. Electrode Filtering Characteristic

CPW electrodes acts as a low-pass filter on the RF data given to the electrode. Based on RF response obtained in the simulation, filter coefficients are generated for the CPW electrodes, and the spectrum is calculated. Figure A2a shows the power spectrum of the filter. For comparison, the power spectrum of an ideal filter with bandwidth 159 GHz is also shown in the figure. Generated bit stream was passed through the designed electrode,

and the output stream is shown in Figure A2b. The effects of filtering are clearly visible on the bit stream in the figure.

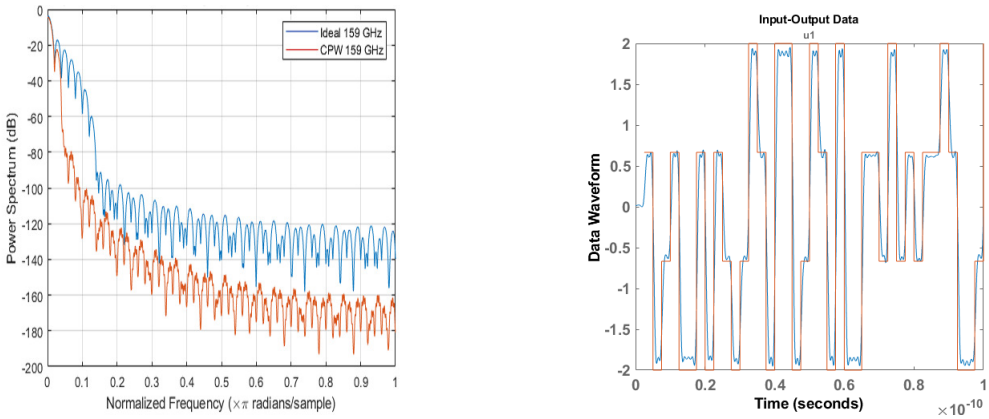

(**a**) (**b**)

Figure A2. (**a**) Power spectrum of Ideal (blue) and CPW Electrode Filters (orange). (**b**) Input and output bitstream.

References

1. Cisco Visual Networking Index: Global Mobile Data Traffic Forecast Update, 2015–2020, 2016, White Paper. Available online: http://www.cisco.com/c/en/us/solutions/collateral/service-provider/visual-networking-index-vnimobile-white-paper-c11-520862.html (accessed on 1 January 2023).
2. Zhang, M.; Wang, C.; Kharel, P.; Zhu, D.; Lončar, M. Integrated lithium niobate electro-optic modulators: When performance meets scalability. *Optica* **2021**, *8*, 652–667. [CrossRef]
3. Marpaung, D.; Yao, J.; Capmany, J. Integrated microwave photonics. *Nat. Photonics* **2019**, *13*, 80–90. [CrossRef]
4. Xu, M.; Cai, X. Advances in integrated ultra-wideband electro-optic modulators. *Opt. Express* **2022**, *30*, 7253–7274. [CrossRef]
5. Orlandi, P.; Morichetti, F.; Strain, M.J.; Sorel, M.; Melloni, A.; Bassi, P. Tunable silicon photonics directional coupler driven by a transverse temperature gradient. *Opt. Lett.* **2013**, *38*, 863–865. [CrossRef]
6. Xu, H.; Li, X.; Xiao, X.; Li, Z.; Yu, Y.; Yu, J. Demonstration and Characterization of High-Speed Silicon Depletion-Mode Mach–Zehnder Modulators. *IEEE J. Sel. Top. Quantum Electron.* **2014**, *20*, 23–32. [CrossRef]
7. Errando-Herranz, C.; Takabayashi, A.Y.; Edinger, P.; Sattari, H.; Gylfason, K.B.; Quack, N. MEMS for Photonic Integrated Circuits. *IEEE J. Sel. Top. Quantum Electron.* **2020**, *26*, 1–16. [CrossRef]
8. Zhu, D.; Shao, L.; Yu, M.; Cheng, R.; Desiatov, B.; Xin, C.J.; Hu, Y.; Holzgrafe, J.; Ghosh, S.; Shams-Ansari, A.; et al. Integrated photonics on thin-film lithium niobate. *Adv. Opt. Photon.* **2021**, *13*, 242–352. [CrossRef]
9. Chen, G.; Lin, H.-L.; Ng, J.D.; Danner, A.J. Integrated Electro-Optic Modulator in Z-Cut Lithium Niobate Thin Film with Vertical Structure. *IEEE Photonics Technol. Lett.* **2021**, *33*, 1285–1288. [CrossRef]
10. Sinatkas, G.; Christopoulos, T.; Silipakos, O.; Kriezis, E.E. Electro-optic modulation in integrated photonics. *J. Appl. Phys.* **2021**, *130*, 010901. [CrossRef]
11. Demkov, A.A.; Bajaj, C.; Ekerdt, J.G.; Palmstrøm, C.J.; Ben Yoo, S.J. Materials for emergent silicon-integrated optical computing. *J. Appl. Phys.* **2021**, *130*, 070907. [CrossRef]
12. Honardoost, A.; Safian, R.; Rao, A.; Fathpour, S. High-Speed Modeling of Ultracompact Electrooptic Modulators. *J. Light. Technol.* **2018**, *36*, 5893–5902. [CrossRef]
13. Gopalaknshnan, G.K.; Burns, W.K.; McElhanon, R.W.; Bulmer, Catherine, H.; Greenblatt, A.S. Performance and Modeling of Broadband LiNb03 Traveling Wave Optical Intensity Modulators. *J. Light. Technol.* **1994**, *12*, 1807–1819. [CrossRef]
14. Rao, A.; Patil, A.; Rabiei, P.; Honardoost, A.; DeSalvo, R.; Paolella, A.; Fathpour, S. High-performance and linear thin-film lithium niobate Mach-Zehnder modulators on silicon up to 50 GHz. *Opt. Lett.* **2016**, *41*, 5700–5703. [CrossRef]
15. Betts, G.E. Linearized modulator for suboctave-bandpass optical analog links. *IEEE Trans. Microw. Theory Tech.* **1994**, *42*, 2642–2649. [CrossRef]
16. Mirza, T.N.; Haxha, S.; Dayoub, I. A Linearized Analog Microwave Photonic Link With an Eliminated Even-Order Distortions. *IEEE Syst. J.* **2021**, *15*, 4843–4851. [CrossRef]
17. Shaqiri, S.; Haxha, S.; Flint, I.; Ademgil, H. Microwave photonics analog link based on two integrated D-DPMZM linearized signals and with eliminated odd harmonics and all IMD's. *Opt. Quant. Electron.* **2022**, *54*, 464. [CrossRef]
18. Wang, C.; Zhang, M.; Chen, X.; Bertrand, M.; Shams-Ansari, A.; Chandrasekhar, S.; Winzer, P.; Lončar, M. Integrated lithium niobate electro-optic modulators operating at CMOS-compatible voltages. *Nature* **2018**, *562*, 101–104. [CrossRef] [PubMed]
19. He, M.; Xu, M.; Ren, Y.; Jian, J.; Ruan, Z.; Xu, Y.; Gao, S.; Sun, S.; Wen, X.; Zhou, L.; et al. High-performance hybrid silicon and lithium niobate Mach–Zehnder modulators for 100 Gbit/s and beyond. *Nat. Photonics* **2019**, *13*, 359–364. [CrossRef]

20. Wang, X.; Weigel, P.O.; Zhao, J.; Ruesing, M.; Mookherjea, S. Achieving beyond-100-GHz large-signal modulation bandwidth in hybrid silicon photonics Mach Zehnder modulators using thin film lithium niobate. *APL Photonics* **2019**, *4*, 096101. [CrossRef]
21. Ahmed, A.N.R.; Shi, S.; Mercante, A.; Nelan, S.; Yao, P.; Prather, D.W. High-efficiency lithium niobate modulator for K band operation. *APL Photonics* **2020**, *5*, 091302. [CrossRef]
22. Liu, Y.; Li, H.; Liu, J.; Tan, S.; Lu, Q.; Guo, W. Low V_π thin-film lithium niobate modulator fabricated with photolithography. *Opt. Express* **2021**, *29*, 6320–6329. [CrossRef]
23. Huang, X.; Liu, Y.; Li, Z.; Guan, H.; Wei, Q.; Yu, Z.; Li, Z. Advanced Electrode Design for Low-Voltage High-Speed Thin-Film Lithium Niobate Modulators. *IEEE Photonics J.* **2021**, *13*, 1–9.
24. Patel, D.; Ghosh, S.; Chagnon, M.; Samani, A.; Veerasubramanian, V.; Osman, M.; Plant, D.V. Design, analysis, and transmission system performance of a 41 GHz silicon photonic modulator. *Opt. Express* **2015**, *23*, 14263–14287. [CrossRef]
25. Simons, R.N. *Coplanar Waveguide Circuits, Components, and Systems*; John Wiley and Sons: Hoboken, NJ, USA, 2001.
26. Chen, E.; Chou, S.Y. Characteristics of Coplanar Transmission Lines on Multilayer Substrates: Modeling and Experiments. *IEEE Trans. Microw. Theory Tech.* **1997**, *45*, 939–945. [CrossRef]
27. Goswami, S.; Thompson, D.; Williams, R.S.; Goswami, S.; Venkatesan, T. Colossal current and voltage tunability in an organic memristor via electrode engineering. *Appl. Mater. Today* **2020**, *19*, 100626. [CrossRef]
28. Hou, Y.; Zhang, X.; Wu, W.; Zhang, T.; Chen, P.; Deng, Z. Controlling the Surface Roughness of Surface-Electrode Ion Trap Based on Micro-Nano Fabrication. *Coatings* **2021**, *11*, 406. [CrossRef]
29. *Current-Tuning, C-Band Ultra-Low-Noise Hybrid Laser (Spec Sheet)*; Thor Labs: Newton, NJ, USA. Available online: https://www.thorlabs.com/newgrouppage9.cfm?objectgroup_id=13653 (accessed on 1 January 2023).
30. Winzer, P.J.; Essiambre, R.-J. Advanced Modulation Formats for High-Capacity Optical Transport Networks. *J. Light. Technol.* **2006**, *24*, 4711–4728. [CrossRef]
31. Melikyan, A.; Kaneda, N.; Kim, k.; Baeyens, Y.; Dong, P. Differential Drive I/Q Modulator Based on Silicon Photonic Electro-Absorption Modulators. *J. Lightwave Technol.* **2020**, *38*, 2872–2876. [CrossRef]